Submitted to The Astrophysical Journal
Preprint typeset using LaTeX style emulateapj v. 10/09/06

arXiv:0704.0643v1 [astro-ph] 4 Apr 2007

MAPPING THE YOUNGEST GALAXIES TO REDSHIFT ONE[1,2]

Yuko Kakazu,[3] Lennox L. Cowie,[3] Esther M. Hu,[3]

Submitted to The Astrophysical Journal

ABSTRACT

We describe the results of a narrow band search for ultra-strong emission line galaxies (USELs) with EW(Hβ) $\geq$ 30 Å. 542 candidate galaxies are found in a half square degree survey using two $\sim$ 100Å filters centered at 8150Å and 9140Å with Subaru/SuprimeCam. Followup spectroscopy has been obtained for randomly selected objects in the candidate sample with KeckII/DEIMOS and has shown that they consist of [O III]λ5007, [O II]λ3727, and Hα selected strong-emission line galaxies at intermediate redshifts ($z < 1$), and Lyα emitting galaxies at high-redshift ($z >> 5$). We determine the Hβ luminosity functions and the star formation density of the USELs, which is 5-10% of the value found from ultraviolet continuum objects at $z = 0 - 1$, suggesting that they correspond to a major epoch in the galaxy formation process at these redshifts. Many of the USELs show the temperature-sensitive [O III]λ4363 auroral lines and about a dozen have oxygen abundances satisfying the criteria of eXtremely Metal Poor Galaxies (XMPGs). These XMPGs are the most distant known today and our high yield rate of XMPGs suggests that narrowband method is powerful in finding such populations. Moreover, the lowest metallicity measured in our sample is 12+log(O/H)=7.06 (6.78−7.44), which is close to the minimum metallicity found in local galaxies, though we need deeper spectra to minimize the errors. HST/ACS images of several USELs exhibit widespread morphologies from relatively compact high surface brightness objects to very diffuse low surface brightness ones. The luminosities, metallicities and star formation rates of USELs are consistent with the strong emitters being start-up intermediate mass galaxies which will evolve into more normal galaxies and suggest that galaxies are still forming in relatively chemically pristine sites at $z < 1$.

Subject headings: cosmology: observations — galaxies: distances and redshifts — galaxies: abundances — galaxies: evolution — galaxies: starburst

1. INTRODUCTION

The study of low-metallicity galaxies is of considerable interest for the clues that it can provide about the first stages of galaxy formation and chemical enrichment. We would also like to know if there are any genuinely young galaxies undergoing their first episodes of star formation at low redshifts. To date, the most metal-poor systems studied have been the blue compact emission-line galaxies found in the local Universe, with systems such as I Zw 18 and SBS 0335-052W defining the low metallicity boundary with measured 12+log (O/H) of $\sim$ 7.1 − 7.2 (Sargent & Searle 1970; Thuan & Izotov 2005; Izotov et al. 2005). More recently, the Sloan Digital Sky Survey (SDSS) has yielded additional extremely metal-poor galaxies (XMPGs) (12+log (O/H) < 7.65 or $Z < Z_{\odot}/12$; Kniazev et al. 2003; Izotov et al. 2006a). Despite enormous efforts, only a few dozen such XMPGs are known, all at redshift $z < 0.05$ (e.g., Oey 2006; Izotov 2006b).

Historically, objective prism surveys have been used to select emission-line galaxies for low-metallicity studies. (e.g. the Hamburg QSO Survey (Popescu et al. 1996) and its HSS sequel (Ugryumov et al. 1999) that discovered HS 2134+0400 (Pustilnik et al. 2006) and the Kitt Peak International Spectroscopy Survey (KISS; Salzer et al. 2000; Melbourne & Salzer 2002)). The advantage of using the objective prism technique rather than the continuum selection, employed with the SDSS (Kniazev et al. 2003) or DEEP2 surveys (Hoyos et al. 2005), is that they have a higher efficiency and provide a more uniform selection. By comparison, continuum/broad-band surveys have a very low yield rate (8 new XMPGs and 4 recovered XMPGS from an analysis of 250,000 spectra over $\sim$3000 deg^2 for the SDSS (Kniazev et al. 2003), since low-metallicity populations in their first outburst have weak continuua and strong emission lines.

An alternative method of discovering strong emission-line, low-metallicity galaxies is to use narrowband surveys. Strong emission-line galaxies have historically been picked up in high-z Lyman alpha searches (e.g., Stockton & Ridgway 1998; Hu et al. 1998, 2004; Stern et al. 2000; Tran et al. 2004; Ajiki et al. 2006) where they have been considered contaminants. However, the low redshift emission line galaxies seen in these surveys are of great interest in their own right as we shall show in the present paper. While some spectroscopic studies have been carried out for low-redshift galaxies selected from narrowband surveys (e.g., Maier et al. 2006; Ly et al. 2007), the small sample sizes have precluded any detailed investigation of metallicity and identification of a low-metallicity population.

The narrowband method probes to much deeper limits than the objective prism surveys. This enables probing star-forming populations out to near redshift $z \sim 1$

---

[1] Based in part on data obtained at the Subaru Telescope, which is operated by the National Astronomical Observatory of Japan.

[2] Based in part on data obtained at the W. M. Keck Observatory, which is operated as a scientific partnership among the the California Institute of Technology, the University of California, and NASA and was made possible by the generous financial support of the W. M. Keck Foundation.

[3] Institute for Astronomy, University of Hawaii, 2680 Woodlawn Drive, Honolulu, HI 96822.

where the cosmic star formation rates are considerably higher. Furthermore the narrow-band emission-line selection can allow us to assemble very large samples of strong-emission line objects, with a clean selection of different line types for the construction of luminosity functions.

Such a sample allows us to address such questions as whether there are substantial populations of strong star-forming galaxies with low metallicities among more massive galaxies. There has been considerable controversy about the interpretation of the low metallicity measurements in the blue compact galaxy samples where the ease with which gas may be ejected in these dwarf galaxies has complicated the picture (e.g., Corbin et al. 2006) or, at least, resulted in identifying low metallicity systems which are not forming their first generation of stars. The identification of low metallicity galaxies – at the level of the XMPGs – among massive galaxies can provides less ambiguous examples of galaxies that are genuinely ‘young’ and caught in the initial stages of star formation. Current efforts to identify low metallicity galaxies from continuum selected surveys (e.g., Kobulnicky et al. 2003; Lilly et al. 2003; Kobulnicky & Kewley 2004; Hoyos et al. 2005) have low-metallicity thresholds that are higher than this – about one-third solar (in O/H). With a narrow-band selection criterion much larger emission-line samples including such low metallicity galaxies can be identified. With these large samples it is also possible to determine whether there is an observed lower metallicity threshold for such galaxies, and to estimate what the contribution of such strong star-formers might be at these epochs.

In the present work we use a number of deep, narrow-band images obtained with the SuprimeCam mosaic CCD camera (Miyazaki et al. 2002) on the Subaru 8.2-m telescope to find a large sample of extreme emission-line galaxies. We first (§2) outline the selection criteria (magnitude and flux thresholds) for the target fields resulting in a sample of 542 galaxies, which we call USELs (Ultra-Strong Emission Liners). We then describe (§3) the spectroscopic followups for 161 of these galaxies using multi-object masks with the DEIMOS spectrograph (Faber et al. 2003) on the 10-m Keck II telescope. Sample spectra for each class of object are shown. Flux calibration and equivalent width distributions are presented in §4, and the resulting measured line ratios are discussed. In §5 luminosity functions are constructed and star formation rates are estimated for the sample. These galaxies are estimated to contribute roughly 10% to the measured star-formation rate (without extinction corrections) at this epoch. Analysis of the metallicities is given in §6. Their morphologies and dynamical masses are discussed in §7 and a final summary discussion is given in §8. We use a standard $H_0 = 70$ km s^{-1} Mpc^{-1}, $\Omega_b = 0.3$, $\Omega_\Lambda = 0.7$ cosmology throughout.

2. THE NARROW BAND SELECTION

The emission line sample was chosen from a set of narrow band images obtained with the SuprimeCam camera on the Subaru 8.2-m telescope. The data were obtained in a number of runs between 2001 and 2005 under photometric or near photometric conditions. We used two ∼120 Å (FWHM) filters centered at nominal wavelengths of 8150 Å and 9140 Å in regions of low sky background between the OH bands. The nominal specifications for the Subaru filters may be found at `http://www.naoj.org/Observing/Instruments/SCam/sensitivi` and are also described in Ajiki et al. (2003). We shall refer to these filters as NB816 and NB912.

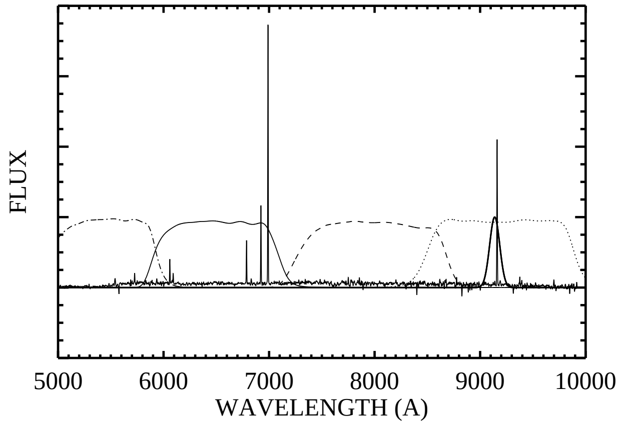

Fig. 1.— Schematic illustration of the selection process and a typical spectrum of the galaxies we find. The objects are chosen based on their excess light in one of two narrow band filters at 8160 Å and 9140Å. The present case corresponds to an Hα emission line object found in the 9140Å filter (shown with the narrow solid curve). Also illustrated are the broad band V (dash-dot), R (solid), I (dashed), and z' (dotted) filters use to measure the continuum. The spectrum shown corresponds to object 205 in Table 3 and is an $H\alpha$ emitter at $z = 0.3983$. The easily visible lines are the Balmer series and the [O III] lines at λλ5007, 4959, and 4363Å.

About 5 hour exposures were obtained with NB816 and ∼10 hour exposures with NB912 yielding 5 sigma limits fainter than 26 mags in both bands. Deep exposures in B, V, R, I and z' were also taken for the fields. The data were taken as a sequence of dithered background-limited exposures and successive mosaic sequences were rotated by 90 degrees. Only the central uniformly covered areas of the images were used. Corresponding continuum exposures were always obtained in the same observing run as the narrowband exposures to avoid false identifications of transients such as high-z supernovae, or Kuiper belt objects, as emission-line candidates. A detailed description of the full reduction procedure for images is given in Capak et al. (2004). All magnitudes are given in the AB system (Oke 1990). These were measured in 3″ diameter apertures, and had average aperture corrections applied to give total magnitudes.

The primary purpose of the program was to study Lyα emitters at redshifts of $z \sim 5.7$ and $z \sim 6.6$ (Hu et al. 2004, 2007) but the narrow band imaging is also ideal for selecting lower redshift emission line galaxies and it is for this purpose that we use these data in the present paper. The fields which we use and the area covered (approximately a half square degree in each bandpass) are summarized in Table 1. These are distributed over the sky to deal with cosmic variance. We selected galaxies in the narrowband NB816 filter using the Cousins I band filter as a reference continuum bandpass and including all galaxies with $NB816 < 25$ and $I - NB816$ greater than 0.8. We selected galaxies in the $NB912$ filter with the z filter as the reference continuum bandpass and included all galaxies with $NB912 < 25$ and $z - NB912$ greater than 1. The selection process is illustrated for

TABLE 1
NARROWBAND SURVEY AREA COVERAGE

Field	RA (J2000)	Dec (J2000)	(l^{II}, b^{II})	E_{B-V}[a]	NB816 (arcmin^2)	NB912 (arcmin^2)
SSA22	22:17:57.00	+00:14:54.5	(63.1,−44.1)	0.07	674	591
SSA22_new	22:18:24.67	+00:36:53.4	(63.6,−43.9)	0.06	278	278
A370_new	02:41:16.27	−01:34:25.1	(173.4,−53.3)	0.03	278	278
HDF-N	12:36:49.57	+62:12:54.0	(125.9,+54.8)	0.01	710	528
Total					1940	1675

NOTE. — An adjacent field to A370_new is a site of a gravitational lensing cluster at $z \sim 0.375$, and was omitted from the suvey.
[a] estimated using `http://irsa.ipac.caltech.edu/applications/DUST/` based on Schlegel et al. (1998)

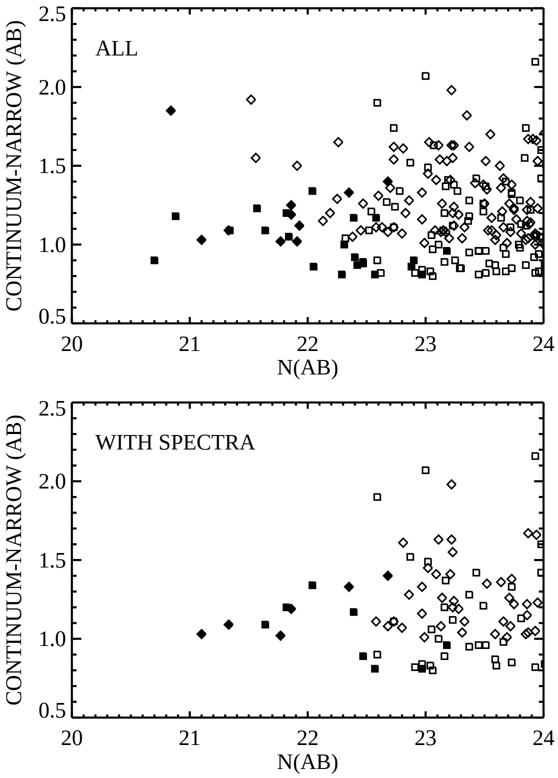

FIG. 2.— Continuum – Narrow band magnitude versus narrow band magitude for all objects with narrow band magnitude brighter than 24. The diamonds show the narrowband excess emission magnitude of the NB912 sample and the squares the NB816 sample. Galaxies which would be included in an $R < 24$ continuum selected sample are shown with solid symbols. The upper panel shows the complete sample while the lower panel shows the subsample which has been spectroscopically identified.

a galaxy found in the NB912 filter in Figure 1. Both selections correspond roughly to choosing objects with emission lines with rest frame equivalent widths greater than 100 Å. The exact equivalent width limit depends on the precise position of the emission line in the filter and the redshift of the galaxy which in turn depends on which emission line is producing the excess light in the narrow band.

The final USEL sample consists of 542 galaxies (267 in the NB816 filter and 275 in the NB912 filter). Tabulated coordinates, multi-color magnitudes, and redshifts (where measured) for these objects are summarized in Table 2. Very few of these objects would be included in continuum-selected spectroscopic samples. Figure 2 shows the narrow band excess as a function of narrowband (N_{AB}) magnitude for objects with narrow band magnitudes brighter than 24. The open symbols show the present sample while the solid symbols show objects which would be included in an $R < 24$ continuum-selected sample.

3. SPECTRA

Spectroscopic observations were obtained for 161 USELs from the sample using the Deep Extragalactic Imaging Multi-Object Spectrograph (DEIMOS; Faber et al. 2003) on Keck II in a series of runs between 2003 and 2006. The emission line objects were included in masks designed to observe high-z Lyα candidates and, as can be seen in the lower panel of Figure 2, constitute an essentially random sample of the emission line galaxies.

The observations were primarily made with the G830 ℓ/mm grating blazed at 8640 Å and used 1″ wide slitlets. In this configuration, the resolution is 3.3 Å, which is sufficient to distinguish the [O II]λ3727 doublet structure. This allows us to easily identify [O II]λ3727 emitters where often the [O II]λ3727 doublet is the only emission feature. The spectra cover a wavelength range of approximately 4000 Å and were centered at an average wavelength of 7800 Å, though the exact wavelength range for each spectrum depends on the slit position with respect to the center of the mask along the dispersion direction. The G830 grating used with the OG550 blocker gives a throughput greater than 20% for most of this range, and $\sim$ 28% at 8150 Å. The observations were not generally taken at the parallactic angle, since this was determined by the mask orientation, so considerable care must be taken in measuring line fluxes as we discuss below. Each $\sim$ 1 hr exposure was broken into three subsets, with the objects stepped along the slit by 1.5″ in each direction. Some USELs were observed multiple times, resulting in total exposure times for these galaxies of 2−3 hours. The two-dimensional spectra were reduced following the procedure described in Cowie et al. (1996) and the final one-dimensional spectra were extracted using a profile weighting based on the strongest emission line in the spectrum. A small number of the spectra were obtained with the ZD600 ℓ/mm grating giving a correspondingly lower resolution but a wider wavelength

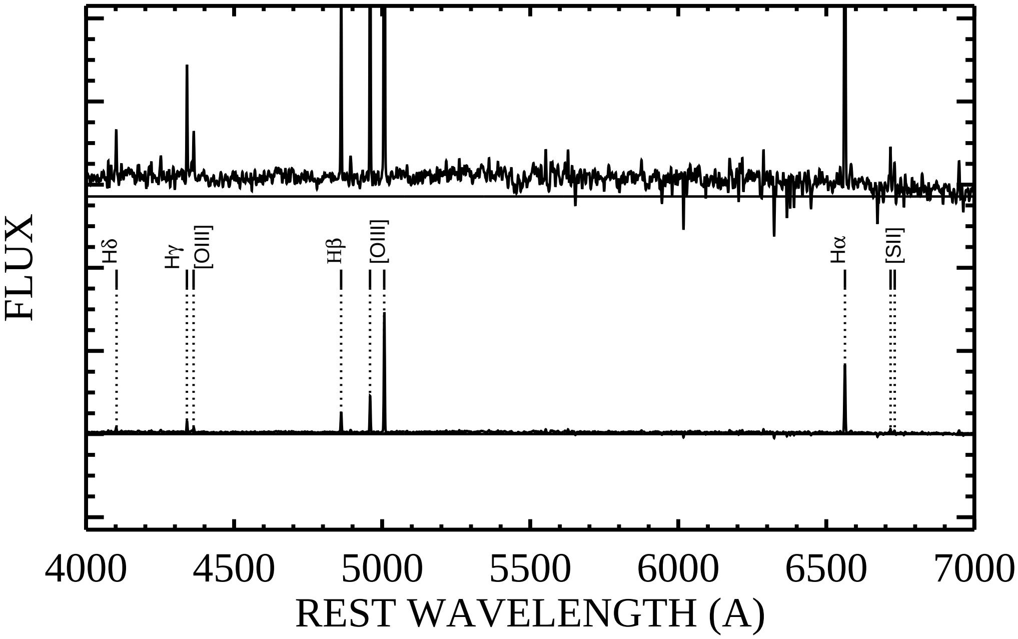

Fig. 3.— Spectrum of an Hα emission galaxy selected in the NB912 filter. In the upper plot we have decreased the scale of the vertical axis by a factor of 10 to show the continuum and the weaker lines. The more important emission line features are labelled and marked with the dotted lines.

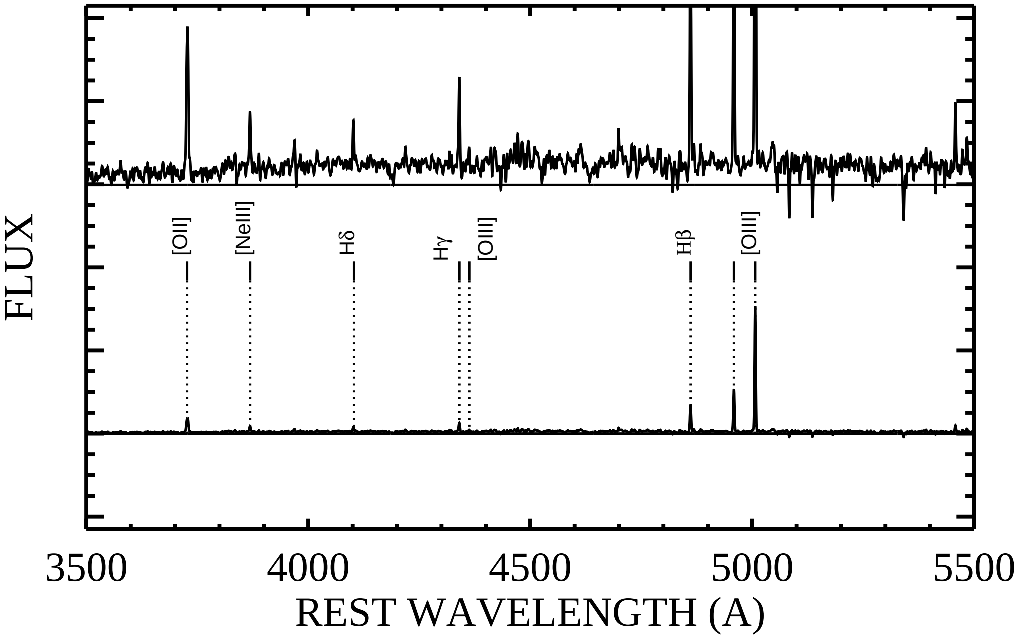

Fig. 4.— Spectrum of an [O III] galaxy in the NB816 selected sample. The lower plot shows the relative strengths of the very strong emission lines in the spectrum. In the upper plot we have decreased the scale of the vertical axis by a factor of 10 to show the continuum and the weaker lines. The more important emission line features are labelled and marked with the dotted lines.

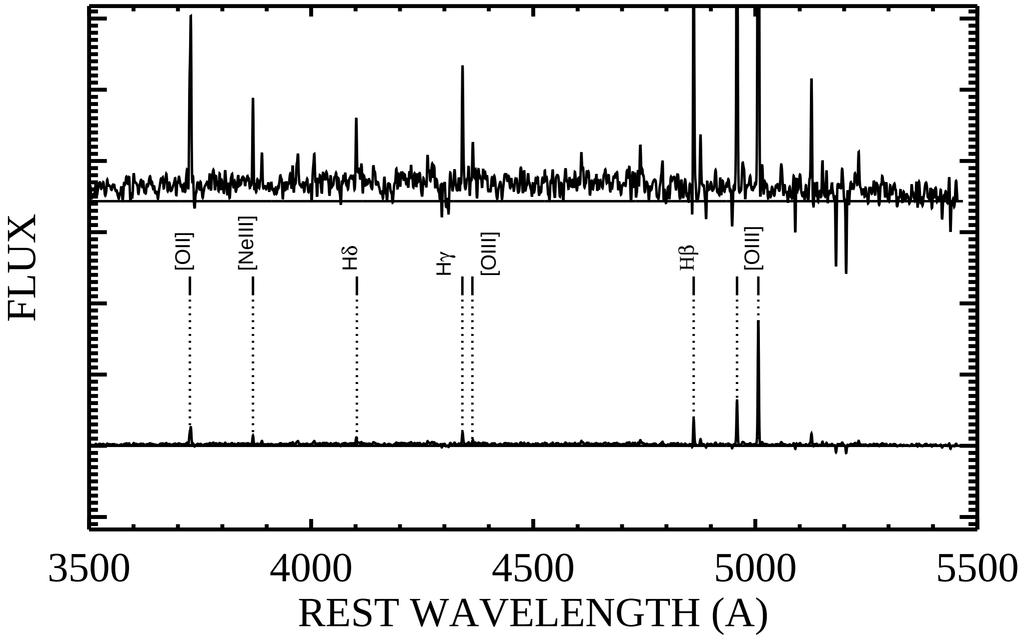

FIG. 5.— Spectrum of an [O III] galaxy selected in the NB912 filter. The lower plot shows the relative strengths of the very strong emission lines in the spectrum. In the upper plot we have decreased the scale of the vertical axis by a factor of 10 to show the continuum and the weaker lines. The more important emission line features are labelled and marked with the dotted lines.

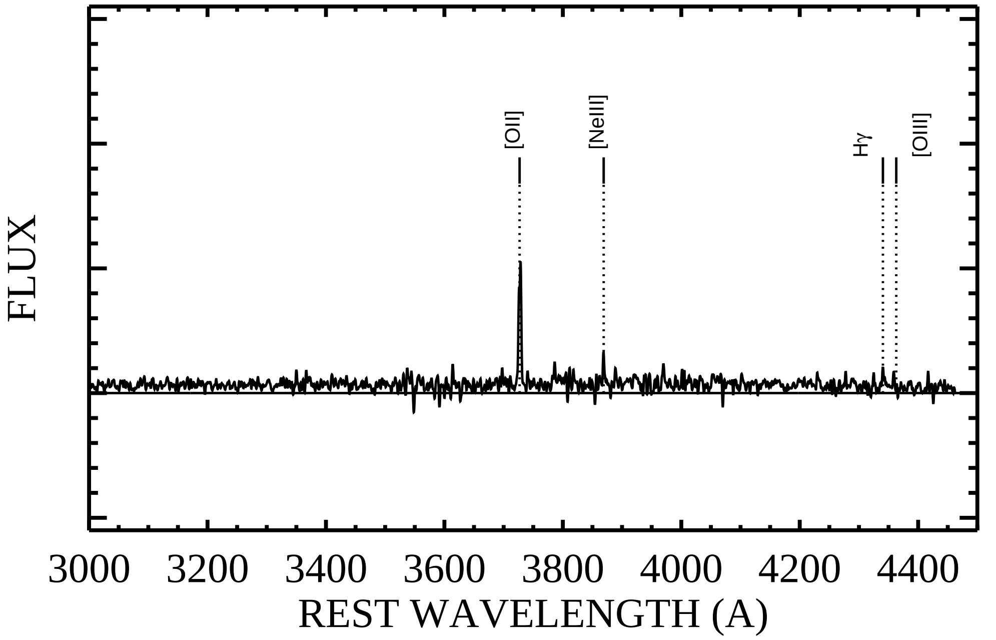

FIG. 6.— Spectrum of an [O II] galaxy selected in the NB816 filter. The plot shows the relative strengths of the very strong emission lines in the spectrum. The more important emission line features are labelled and marked with the dotted lines.

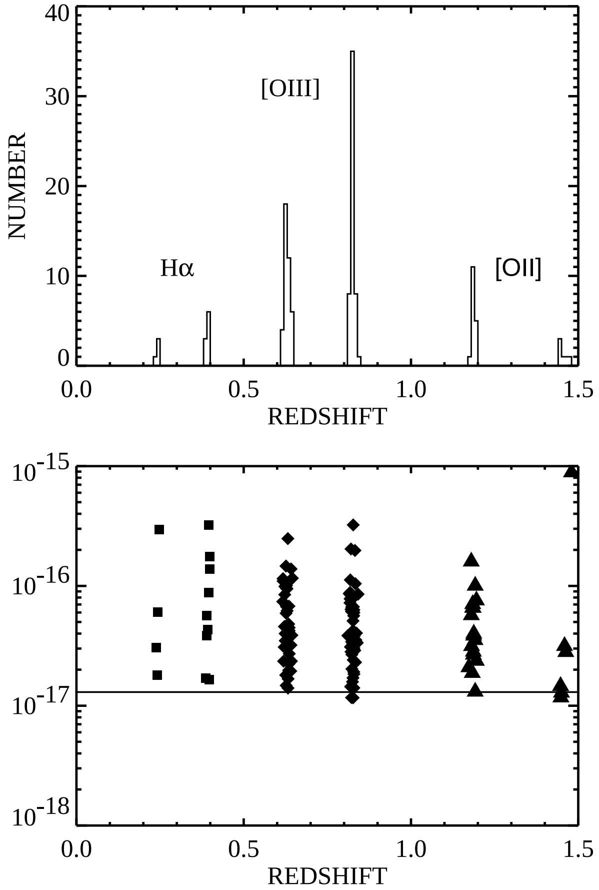

Fig. 7.— (a) Distribution of redshifts for the spectroscopically identified sources. [O III] λ5007 emitters are the most common. Since the focus of this paper is on intermediate-redshift ($z \lesssim 1$) strong emission line galaxies, we did not plot high redshift Lyα galaxies ($z >> 5$) in our NEO sample. High-z Lyα emitters are discussed in Hu et al. (2004, 2007). (b) Flux versus redhift for the spectroscopically identified sample. Squares are Hα, diamonds are [O III] λ5007, and triangles are [O II] λ3727. The solid line shows the flux limit corresponding to the narrow band magnitude limit of N(AB)=25 for an emitter with very large equivalent width. Some objects with lower equivalent widths fall below this limit.

coverage. These observations were centered at 7200 Å.

Essentially all of the emission line candidates which were observed were identified, though two of the objects in the NB816 sample are stars where the absorption line structure mimics emission in the band. Sample spectra are shown in Figures 3, 4, 5, and 6. The measured redshifts are given in Tables 2 and 3. The narrow band emission line selection produces a mixture of objects corresponding to Hα, [O III]λ5007, and [O II]λ3727 and, at the faintest magnitudes (> 24), high redshift Lyα emitters. The number of objects seen in each line and the redshifts where they are found are shown in Figure 7. The spectroscopically identified sample from both bands contains 13 Hα, 92 [O III]λ5007, and 23 [O II]λ3727 emitters. In the remainder of the paper we shall focus primarily on the Hα and [O III]λ5007 selected galaxies which lie between redshifts zero and one.

Since only 30% of the USELs are spectroscopically identified we must apply a substantial incompleteness correction in computing the line luminosity function and the universal star formation histories. Because the type mix may vary as a function of magnitude we have adopted a magnitude dependent weighting for each galaxy equal to the total number of galaxies at this magnitude divided by the number of spectroscopically identified galaxies. However, the analysis is not particularly sensitive to the adopted scheme since the fraction of identified galaxies is relatively constant with magnitude.

4. FLUX CALIBRATIONS

Generally our spectra were not obtained at the parallactic angle since this is determined by the DEIMOS mask orientation. Therefore flux calibration using standard stars is problematic due to atmospheric refraction effects, and special care must be taken for the flux calibration. We thus employed three independent methods for the flux calibration. In §4.1 we introduce “primary fluxes” which are absolute fluxes of the emission lines used to select the galaxies. Primary fluxes are computed from the SuprimeCam broadband and narrowband magnitudes. We use these fluxes to derive luminosity functions of Hα and [O III]λ5007 emitters at $z < 1$ (§5.1).

In §4.2 we measure line fluxes from the spectra. Relative line fluxes can be measured from the spectra without flux calibration as long as we restrict the line measurments to over short wavelength range where the DEIMOS response is essentially constant. For example, one can assume the response of neighboring lines (e.g. [O III]λ4949 and [O III]λ5007) are the same and therefore one can measure the flux ratio without calibration. For bright galaxies, we can absolutely calibrate the fluxes by integrating spectra and equating them to Subaru broadband fluxes. These line fluxes derived from the spectra are used as a check of the primary fluxes. We show that the ratio of [O III]λ5007/[O III]λ4959 is indeed close to 1/3, and that the fluxes computed from the spectra are highly consistent with the primary fluxes measured in §4.1. In §4.3, we show Balmer flux ratios f(Hβ)/f(Hα) of bright Hα emitters are close to the Case B conditions, suggesting very little reddening.

Metallicity measurements by the direct method require four emission lines that are widely displaced over the spectral wavelength range ([O III]$\lambda\lambda$4959, 5007, [O III]λ4363, and [O II]λ3727). To calibrate these lines, we used neighboring Balmer lines with the assumption of Case B conditions, and this is described in §4.4.

4.1. *Narrow Band Fluxes – Primary Fluxes*

For the emission lines used to select each galaxy we may compute the equivalent widths and absolute fluxes directly from the narrow band magnitudes (N) and the corresponding continuum magnitudes (C) from our SuprimeCam imaging data. For example, in the case of the NB816 selected emission-line galaxies, N corresponds to the NB816 magnitude and C is the I band magnitude. We shall refer to the values calculated in this way as the *primary fluxes* and use this quantity to compute the luminosity functions for each emitter in §5.1.

Defining the quantity

$$R = 10^{-0.4*(N-C)}$$

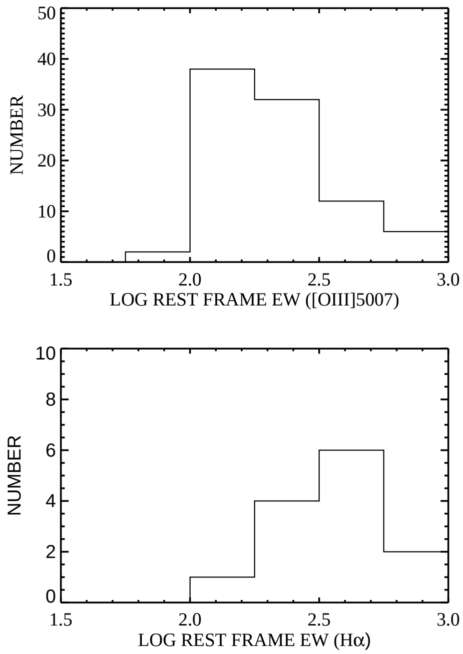

Fig. 8.— (a) Distribution of the rest frame equivalent widths determined from the narrow band magnitudes for the spectroscopically identified [O III] λ5007 sources. (b) Distribution of the rest frame equivalent widths for the Hα selected sample.

the observed frame equivalent width becomes

$$EW = \left[\frac{R-1}{\phi - \dfrac{R}{\Delta\lambda}} \right]$$

where ϕ is the narrow band filter response normalized such that the integral over wavelength is unity and $\Delta\lambda$ is the effective width of the continuum filter. The narrow band filter is often assumed to be rectangular in which case ϕ becomes $1/\delta\lambda$ where $\delta\lambda$ is the width of the narrow band but as can be seen from Figure 1 this is not a very good approximation in the present case. For very high equivalent width objects the denominator in this equation becomes uncertain unless the broad band data are very deep, and this can result in a large scatter in the very highest equivalent widths where the continuum is poorly determined.

In the case of the [O III]λ5007 line we must include the second member of the doublet which also lies within the narrow band filter. We have computed these cases assuming the flux of the [O III]λ4959 line is 0.34 times that of the [O III]λ5007 line. Then $\phi = \phi_1 + 0.34 \times \phi_2$ where ϕ_1 is the filter response at the redshifted 5007 Å wavelength and ϕ_2 is the filter response at redshifted 4959 Å.

The distribution of the rest frame equivalent widths for the Hα and [O III]λ5007 samples is shown in Figure 8. The [O III]λ5007 sample selects objects with rest frame equivalent widths above about 100Å while the lower redshift Hα sample selects objects with rest frame equivalent widths above about 150Å. Since the [O III]λ5007 lines are also generally stronger than the Hα lines the [O III] selection chooses less extreme objects than the Hα selection and will include a larger fraction of galaxies at the given redshift.

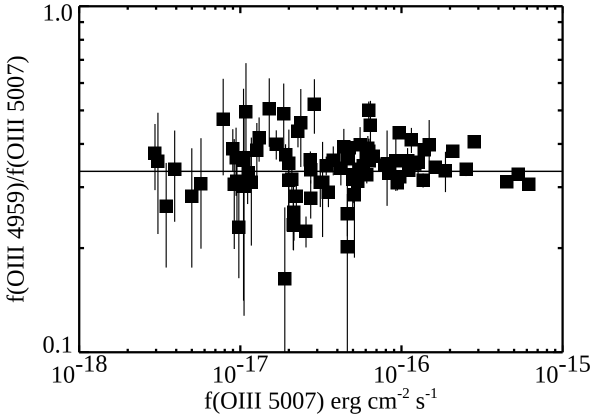

Fig. 9.— The ratio of the [O III] λ4959 line to [O III] λ5007. The errors are plus and minus 1 sigma. The median ratio is 0.338 and the scatter around this value is consistent with that expected from the statistical errors.

The high observed frame equivalent widths make the line fluxes insensitive to the continuum determination and these may simply be found from

$$f = A \left[\frac{10^{-0.4N} - 10^{-0.4C}}{\phi - \dfrac{1}{\Delta\lambda}} \right]$$

where A is the AB zeropoint at the narrow band wavelength in units of erg cm^{-2} s^{-1} Å^{-1}. The flux depends on the filter response at the emission line wavelength and correspondingly is most uncertain at the edges of the filters where this quantity changes rapidly. Primary fluxes defined here are measured by using narrowband (N) and broadband (C) magnitudes from Subaru imaging data with the object redshift information from Keck spectra for the filter response at the exact location of emission line wavelength (ϕ). We use these primary fluxes to construct the luminosity functions of Hα and [O III]λ5007 selected emitters as we discuss in §5.1.

4.2. *Line Fluxes from the Spectra*

For the short wavelength range where DEIMOS response is essentially constant, we may also compute the relative line fluxes from the spectra without calibration. For each spectrum we fitted a standard set of lines. For the stronger lines we used a full Gaussian fit together with a linear fit to the continuum baseline. For weaker lines we held the full width constant using the value measured in the stronger lines and set the central wavelength to the nominal redshifted value. We also measured the noise as a function of wavelength by fitting to random positions in the spectrum and computing the dispersion in the results.

These fits should provide accurate relative fluxes over short wavelength intervals where the DEIMOS response is similar, but may be expected to be poorer over longer wavelength intervals where the true calibration can vary from the adopted value. We tested the relative flux calibration for neighboring lines and the noise measurement by measuring the ratio of the [O III]λ4959/ [O III]λ5007 lines. This is expected to have a value of approximately 0.34. The ratio is shown as a function of the [O III]λ5007 flux in Figure 9. The measured values scatter around the

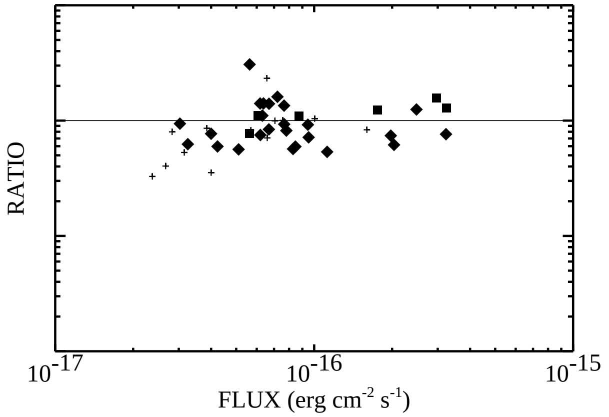

FIG. 10.— Ratio of fluxes computed from the spectra and the broad band magnitudes versus those from the narrow band magnitudes. Hα lines are shown as solid boxes, [O III] λ5007 lines as diamonds and [O II] λ3727 lines as crosses.

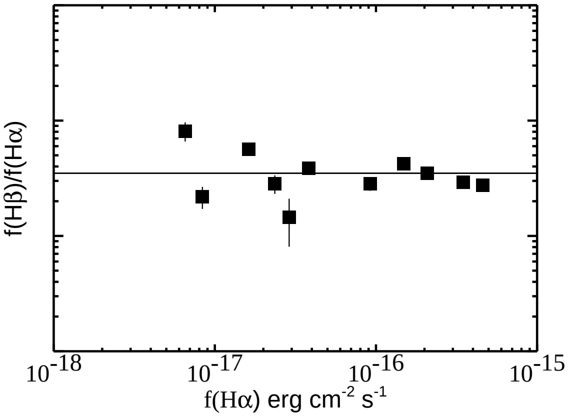

FIG. 11.— The ratio of the Hβ/Hα fluxes versus Hα flux. The values average to the unreddened Balmer decrement shown by the solid line but at the lower fluxes the scatter is larger than expected from the statistical errors reflecting the calibration uncertainties for the fainter sources. The figure shows the ten objects detected in the Hα line with continuum magnitudes above 24.5 in the bandpasses corresponding to the lines.

expected value and the dipsersion is consistent with the noise determination. This result supports our assumption of [O III]λ4959/[O III]λ5007 = 0.34 in the primary fluxes measurements described in §4.1.

The brighter objects may be absolutely calibrated using the continuum magnitudes obtained from our Subaru data. We integrated the spectrum convolved with each SuprimeCam filter response and set this equal to the broad band flux to normalize the spectrum in each of the filters. We then used the Gaussian fits to obtain the spectral line fluxes for lines lying within that broad band. This procedure only works for sources with well determined continuum magnitudes ($C < 24.5$) where the sky subtraction can be well determined in the spectra. For these objects the spectrally determined fluxes are shown versus the primary fluxes in Figure 10 where we plot the ratio of the spectral to the primary flux versus the primary line flux. The values agree extremely well though the measured spectral line fluxes are on average about 80 − 90% of the primary flux values. This may reflect a selection bias in the choice of the objects or the narrow band filters could be slightly narrower than the nominal profiles.

4.3. *Balmer Ratios*

We now measured the Balmer ratios for the sample of objects selected in Hα and where the continuum magnitudes were bright enough to absolutely flux calibrate the spectra. The ratio of f(Hβ)/f(Hα) is shown in Figure 11. The values average closely to the Case B ratio which is shown as the solid line and at brighter fluxes the individual values also closely match to this value suggesting that the galaxies have very little reddening. However, at fainter fluxes the scatter about the average value is considerably higher than the statistical errors. At the faintest fluxes it appears that the systematic uncertainty can be as high as a multiplicative factor of two.

4.4. *Final Flux Calibration for Metallicity Analysis*

For the metallicity analysis we adopted the procedure of normalizing the longer wavelength lines ([O III]$\lambda\lambda$4959, 5007, [O III]λ4363) to their nearest Balmer line to determine the unreddened fluxes. For example, in the case of the Hα emission selected galaxies, we can measure Hα absolute fluxes by the primary fluxes method described in §4.1. We can then derive Hβ and Hγ fluxes from Hα fluxes by assuming Case B recombination [e.g., f(Hα) = 2.85 × f(Hβ), f(Hγ) = 0.469 × f(Hβ) at T = 10^4 K and $N_e \sim 10^2 - 10^4 \mathrm{cm}^{-3}$; Osterbrock 1989]. As H$\beta$ and [O III]$\lambda\lambda$4959, 5007 have very similar DEIMOS response, the relative fluxes should remain the same with or without the flux calibration and this can be expressed by a simple equation:

$$\frac{f_0(\mathrm{H}\beta)}{f_0([\mathrm{O\,III}]\lambda 4959, \lambda 5007)} = \frac{f(\mathrm{H}\beta)}{f([\mathrm{O\,III}]\lambda 4959, \lambda 5007)}$$

where f_0(Hβ) and f_0([O III]λ4959, λ5007) are the flux counts in the un-calibrated, reddened DEIMOS spectra, while f(Hβ) and f([O III]λ4959, λ5007) are absolute, unreddened fluxes. Since we know f(Hβ) from f(Hα) with the Case B assumption and f_0(Hβ)/f_0([O III]λ4959, λ5007) from the DEIMOS spectra, we can derive f([O III]λ 4959, λ5007) using this simple formula. Similary, we can absolutely calibrate [O III]λ4363 lines by using its neighboring Balmer line, Hγ:

$$\frac{f_0(\mathrm{H}\gamma)}{f_0([\mathrm{O\,III}]\lambda 4363)} = \frac{f(\mathrm{H}\gamma)}{f([\mathrm{O\,III}]\lambda 4363)}$$

where f_0(Hγ) and f_0([O III]λ4363) are again the counts in flux uncalibrated, reddened DEIMOS spectra, and f(Hγ) and f([O III]λ4363) are absolute fluxes.

In the case of the [O III] selected emitters, we first derive [O III]$\lambda\lambda$4959, 5007 absolute fluxes using the primary fluxes method (§4.1), and then use the above formula to get absolute fluxes of Hβ, then Hγ (by the Case B ratio), and finally [O III]λ4363.

This flux calibration technique using neighboring Balmer line should work well for the [O III]$\lambda\lambda$4959, 5007, λ4363 lines and the [N II] lines which all lie close to Balmer lines but may be slightly more approximate for the [S II] lines. The higher order Balmer lines are too uncertain to apply this procedure due to inadequate S/N of the lines, and we have used the continuum flux calibrated values with no reddening for the [O II]λ3727 and [Ne III] lines. These values will have correspondingly higher flux

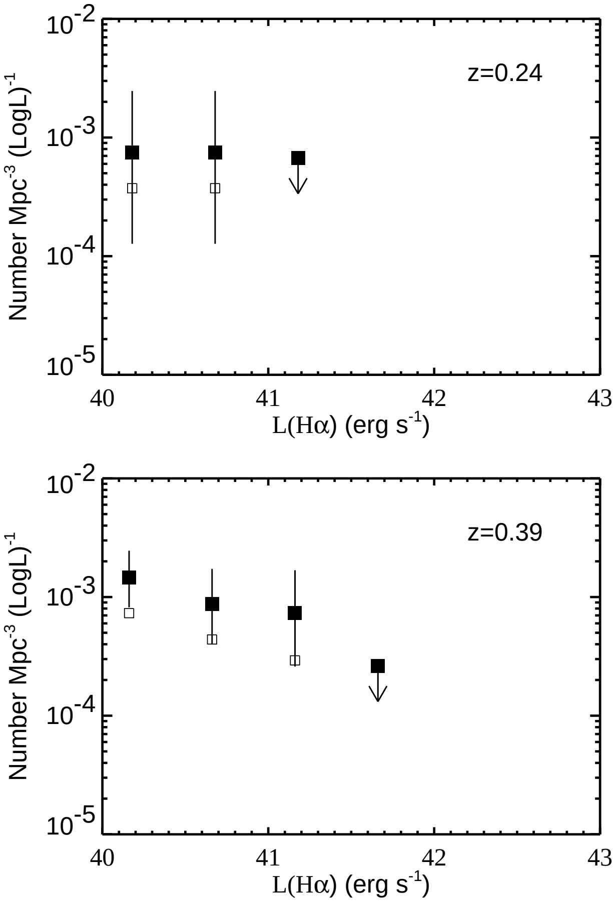

FIG. 12.— The luminosity function of Hα at $z = 0.24$ (top panel) and at $z = 0.39$ (bottom panel). In each case the open boxes show the luminosity functions determined from the spectroscopic sample alone while the solid boxes show the function corrected for the incompleteness in the spectroscopic identification. The errors are plus and minus 1 sigma and at the highest luminosity we show the 1 sigma upper limit.

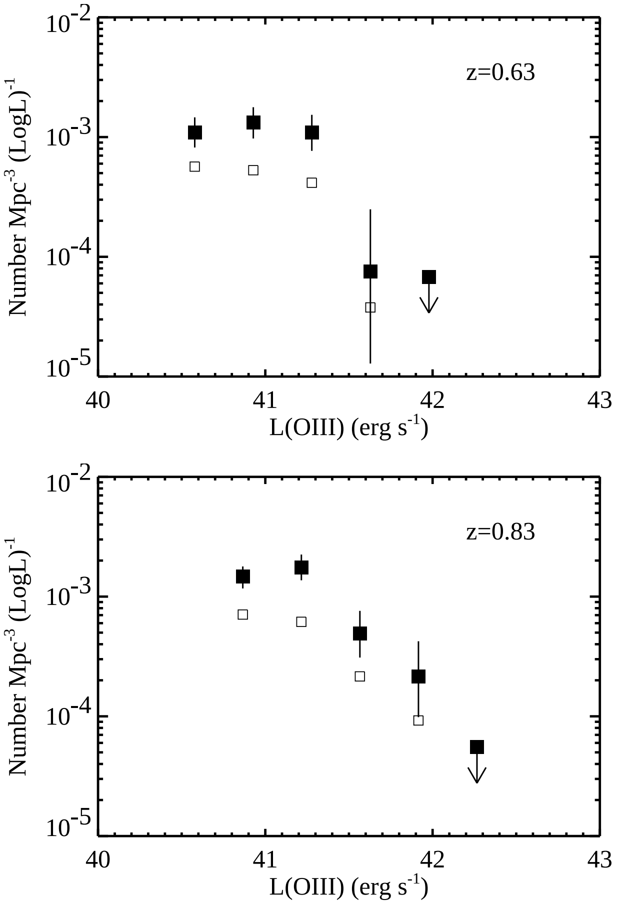

FIG. 13.— The luminosity function of [O III] λ5007 emitters at $z = 0.63$ (top panel) and at $z = 0.83$ (bottom panel). In each case the open boxes show the luminosity functions determined from the spectroscopic sample alone while the solid boxes show the function corrected for the incompleteness in the spectroscopic identification. The errors are plus and minus 1 sigma and at the highest luminosity we show the 1 sigma upper limit.

uncertainties. Fortunately the [O II]λ3727 line is very weak in most of the objects and the uncertainty has little effect on the metallicity determinations. However, ionization analyses based on the [Ne III] line should be undertaken with caution.

5. STAR FORMATION HISTORY

5.1. *Hα and [O III]λ5007 Luminosity Functions*

Because of the high observed frame equivalent widths the primary fluxes are insensitive to the continuum determination. However, they do depend on the filter response at the emission line wavelength so we first restrict ourselves to redshifts where the nominal filter response is greater than 70% of the peak value. This also has the advantage of providing a uniform selection and we assume the window function is flat over the defined redshift range. Now the volume is simply defined by the selected redshift range for all objects above the minimum luminosity which we take as corresponding to a flux of 1.5×10^{-17} erg cm^{-2} s^{-1} (Figure 7). The luminosity function is now obtained by dividing the number of objects in each luminosity bin by the volume. The incompleteness corrected luminosity function is obtained from the sum of the weights in each luminosity bin divided by the volume. The 1 sigma errors shown are calculated from the Poissonian errors based on the number of objects in the bin. The calculated Hα luminosity function is shown for the two redshift ranges corresponding to the NB816 and NB912 selections in Figure 12 and the corresponding [O III]λ5007 luminosity functions in Figure 13.

5.2. *Star Formation Rates*

The individual objects have Hα luminosities stretching up to about 3×10^{41} erg s^{-1} where, at the higher redshifts, we use the Hβ luminosity to infer the Hα value assuming there is no reddening. For a steady formation this would require a star formation rate of a few solar masses per year if we adopt the Kennicutt (1998) conversion rate for his Salpeter mass function.

Since the objects are more probably caused by starbursts the true star formation rate will depend on the evolutionary history. However, the Hα luminosity density should give a reasonable estimate of the universal star formation density of the objects provided only that most of the ionizing photons are absorbed in the galaxies. We first formed the total Hα or Hβ luminosity density of the galaxies by summing over the incompleteness weighted luminosities in each redshift interval. We only included detected objects and did not attempt to extrap-

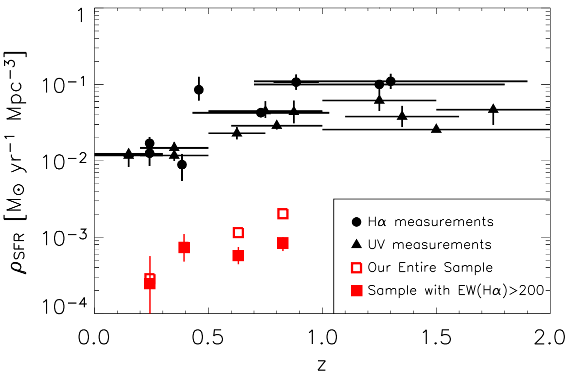

Fig. 14.— The star formation history inferred from the Hα or Hβ luminosity density as a function of redshift. The data from our sample are shown in red. The open squares show the total rate from the entire sample while the solid squares show the values for objects with Hα rest frame equivalent widths in excess of 200Å or Hβ rest frame equivalent widths in excess of 70Å. The diamonds show the UV star formation rates (uncorrected for extinction) from the ground based work of Wilson et al. (2002) and the triangles the Galex results of Wyder et al. (2005) and Schiminovich et al. (2005). Hα measurements from the literature as summarized in Ly et al. (2007) are shown with filled circles. In all cases the errors are $\pm 1\sigma$.

olate to lower luminosities but the result are not particularly sensitive to this because the luminosity functions are relatively flat at the lower luminosities (Figures 13 and 14). We then converted these to star formation rates with the Kennicutt (1998) conversion.

The results are shown in Figure 14. We first plot the rate for the total samples at each redshifts shown by the open squares. We have shown star formation rates for UV continuum samples for comparison and the present sample of strong emitters gives star formation rates which are about 10% of the UV values over the redshift interval. For comparison, we also show the star formation rates from Hα selected samples reported in the literature and summarized in Ly et al. (2007). In order to better understand the evolution we have also restricted our own sample to objects with rest frame equivalent widths of Hα in excess of 200Å at low redshifts and Hβ equivalent widths in excess of 70Å at the higher redshifts. The star formation rates for this sample are shown with the solid squares. This provides a more uniform selection with redshift and gives a slower increase than the total inferred star formation rate. For this sample the SFR is evolving roughly as $(1+z)^3$ broadly similar to other UV and optically determined formation rates in this redshift interval. These more restricted objects comprise about 5% relative to the UV star formation rates at the higher redshifts.

6. GALAXY METALLICITIES

6.1. *[O III] emitters*

The spectra are of variable quality and, in order to measure the metallicities, we need very high signal to noise observations. It is also important that Balmer lines are well detected since our flux calibrations are done using the neighboring Balmer lines (§4.4). We therefore restricted ourselves to [O III] emitters whose Hβ fluxes are detected above 15 sigma. Among 92 [O III] emitters in our total spectroscopic sample, 8 such [O III] emitters were chosen in the NB912 sample, and 10 in the NB816. These emitters have Hγ detected above 4 sigma. Tables 4 and 5 give the oxygen line fluxes normalized by their Hβ fluxes for the NB816 and NB912 selected emitters, respectively. 1σ upper limits are listed when the measured flux is below 1σ.

The most direct method to estimate the gas-phase oxygen abundance is to use the electron temperature of the HII region. Higher gas metallicity increases nebular cooling, leading to lower electron temperatures. Therefore electron temperature is a good indicator of the gas metallicity. The electron temperature can be derived from the ratio of the [O III]λ4363 auroral line to [O III]λλ5007,4959. This procedure is often referred to as the 'direct' method or T_e method (e.g., Seaton 1975; Pagel et al. 1992; Pilyugin & Thuan. 2005; Izotov et al. 2006c). One well-known problem with the direct method, however, is that [O III]λ4363 is generally very weak even in the low-metallicity galaxies. For higher metallicity systems, the far-IR lines become the dominant coolant and therefore the optical auroral line is essentially not detectable. However, the majority of our sample exhibit [O III]λ4363, already suggesting that these are metal-deficient systems. To derive T_e[O III] and the oxygen abundances, we used the Pagel et al. (1992) calibrations with the T_e[O II]$-$$T_e$[O III] relations derived by Garnett (1992). The results are shown in Table 4 (for NB816 selected [O III] emitters) and Table 5 (for NB912 selected [O III] emitters). The Izotov et al. (2006c) formula, which was developed with the latest atomic data and photoionization models, gives consistent abundances within 0.1 dex. The [S II]λλ6717, 6731 lines that are usually used for the determination of the electron number density, are beyond the Keck/DEIMOS wavelength coverage for our [O III] emitters. Therefore we assumed $n_e = 100$ cm^{-3}. However the choice of electron density has little effect as electron temperature is insensitive to the electron density; we get the same results even when we use $n_e = 1000$ cm^{-3}.

The 1σ upper and lower limits on T_e[O III] and the oxygen abundances are also shown in the tables. Because the [O III]λ4363 flux is weak ($< 4\sigma$), the range of our metallicity measurements are quite wide. However, of 18 [O III] emitters, even the upper metallicity limits on 6 emitters satisfy the definition of XMPGs [12 + log(O/H) $<$ 7.65; Kunth & Östlin 2000]. All our emitters, except the ones that only have lower limits on metallicties such as ID31 in Table 4, have very low metallicities – even the *upper* metallicity limits are about 0.02 - 0.2 $Z_\odot$. A few emitters may even have metallicities that are comparable to the currently known most metal-poor galaxies [I Zw 18 and SBS0335−052W; 12 + log(O/H) $\sim$ 7.1 $-$ 7.2]. However our current metallicity errors are too large to measure the baseline metallicity accurately and higher S/N spectra will be necessary for this purpose.

Our discovery rate of XMPGs appers to be significantly higher than those of other surveys. Only 14 new XMPGs have been discovered from the analysis of $\sim$530,000 galaxy spectra in the SDSS and they are all located nearby ($z < 0.005$) (SDSS DR3: Kniazev et al. 2003, SDSS DR4: Izotov et al. 2006a). At higher redshift, 17 metal-poor ($7.8 < 12 + \log({\rm O/H}) < 8.3$) galaxies have been found at $z \sim 0.7$ in the initial phase of the

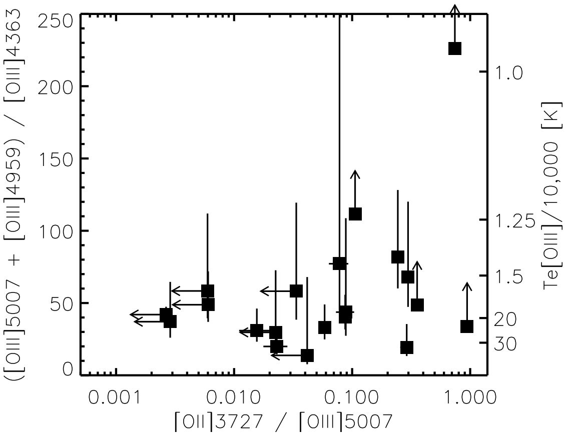

FIG. 15.— [O III]λ4959+λ5007/[O III]λ4363 versus [O II]λ3727/[O III]λ5007 for the [O III] and Hα selected emitters in Table 4 and 5. The electron temperature of the HII region is also shown.

DEEP2 survey of 3,900 galaxies and the Team Keck Redshift Survey of 1,536 galaxies (Hoyos et al. 2005). But none of these galaxies satisfies the condition of XMPGs.

The present sample may be the first XMPGs at intermediate redshift ($z \sim 1$) whose oxygen abundances are securely measured by the direct method. The narrow-band method is very powerful for finding not only high-redshift ($z >> 5$) galaxies, but also strong emission-line, extremely metal-deficient galaxies at intermediate redshifts ($z < 1$).

Figure 15 shows the electron temperature sensitive line ratio, [O III](λ4959+λ5007)/[O III]λ4363 versus [O II]λ3727/[O III]λ5007. If we have an estimate of the metallicity, as in the present case, we can use the [O II]λ3727/[O III]λ5007 ratio to estimate the ionization parameter q. The ionization parameter q is defined as the number of hydrogen ionizing photons passing through a unit area per second per unit hydrogen number density (Kewley & Dopita 2002). For the low metallicity systems with strong [O III]λ4363 lines, we can see from Figure 15 that [O II]λ3727 is very weak compared to [O III]λ5007 with values ranging downwards from 0.3. Assuming the metallicity is less than 0.2 $Z_\odot$ this would place a lower bound of $q = 10^8$ cm s^{-1} on the ionization parameter based on the Kewley & Dopita (2002) model. The higher metallicity objects have stronger [O II]λ3727/[O III]λ5007 which, while in part due to the metallicity, also requires these objects to have lower ionization parameters suggesting we are seeing an evolutionary sequence.

6.2. *Hα emitters*

Among 13 Hα emitters in our spectroscopic sample, only 3 NB912 selected emitters have Hβ fluxes adequate ($> 15\sigma$) for the purpose of metallicity measurements. Their T_e[O III] and oxygen abundances were measured using the direct method described above, and are shown in the Table 5 together with the data for the [O III] emitters. The [O II]λ3727 line of ID266 is outside the Keck/DEIMOS wavelength coverage. In order to derive an upper-limit on the metallicity, we assumed [O II]λ3727/[O III]λ5007 = 1.0, which is the maximum value in our sample (see, Fig. 15). All our Hα emitters are metal poor ($Z_{\rm upper} < 0.45\ Z_\odot$), but none of them are XMPGs.

6.3. *Composite Spectrum*

As can be seen in Figure 15 the objects with low [O II]λ3727/[O III]λ5007 have relatively uniform values of ([O III]λ5007+λ4959)/[O III]λ4363 and similar metallicities. Given the relatively low signal to noise of the individual spectra it therefore seems of interest to form a composite spectrum. Such a spectrum will have weightings on the lines which depend on the individual ionization parameters and metallicity but will give a rough estimate of the average metallicity and temperature of the sample.

In Figure 16 we show the composite spectrum of the 8 objects with [O II]λ3727/[O III]λ5007 less than 0.1. The [O III]λ4363 is now strongly detected with a value of 16.7 ± 2.1 or eight sigma. The mean temperature is $19,500 \pm 1,500$ K and the average abundance 12+log(O/H)=7.5 ± 0.1 and the mean rest frame equivalent width of Hβ is 57Å. The results are similar to the values obtained by averaging the individual analyses of the eight objects.

7. MORPHOLOGIES

The morphology of the USELs may give us a clue to the mechanism of their high star formation activity (SFR $\sim$ a few $M_\odot$/yr) and star formation history; what has triggered the star formation – mergers, gas infall, or galactic winds? High resolution HST/ACS images are available for GOODS-North (GOODS-N) region (Giavalisco et al. 2004) which is one of our survey fields. There are 17 NB816 selected USELs in the GOODS-N, and 16 in the NB912 sample. Figures 17 and 18 show thumbnails of the NB816 and NB912 selected USELs in the GOODS-N field (respectively) with each thumbnail $12''.5$ on a side. The white dashes point to the largest galaxy. We used continuum broadband images to show underlying stellar populations: HST/ACS B, V, z'-band images were used for NB816 emitters, and B, V, I-band for NB912 emitters. High-redshift Lyα emitters ($z >> 5$) are very red because of the continuum absorption below Lyα emission caused by neutral hydrogen in the intergalactic medium. We do not have spectra for most of the USELs in the GOODS-N field yet, and none of the USELs in GOODS-N have metallicity measurements either due to lack of spectra or low spectral S/N. But we can qualitatively argue that the USELs at intermediate redshift ($z < 1$) exhibit widespread morphologies from relatively compact high surface brightness objects to very diffuse low surface brightness ones.

8. DISCUSSION

The present emitters differ from the local dwarf HII galaxies in a large number of ways though they appear much more similar to the XMPGs found in the SDSS samples. They are much more luminous, have large [O III]/[O II] ratios, and they are a relatively high fraction (about 10% by number from Figure 13) of other galaxy populations at these redshifts. Taken together this suggests that we are seeing much more massive galaxies in the early stages of formation and, since we need these to have relatively long lifetimes in order to

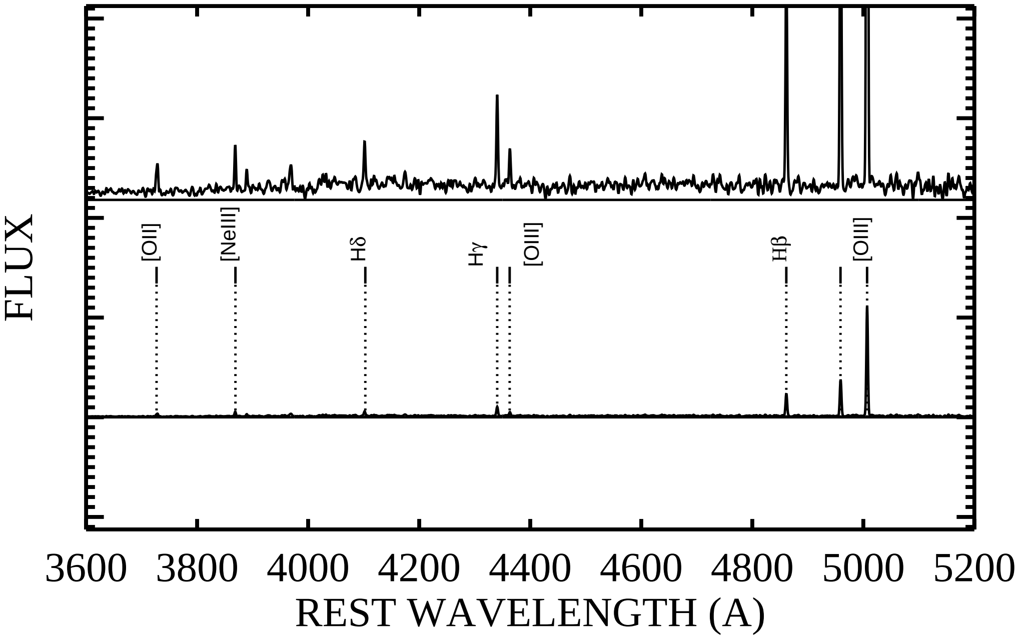

FIG. 16.— Composite spectrum of the 8 emitters with [O II]λ3727/[O III]λ5007 less than 0.1. The eight spectra have simply been summed without weighting. The lower panel shows the stronger lines and the upper the continuum and the weaker lines. The stronger emission lines are labelled and marked with the vertical dotted lines.

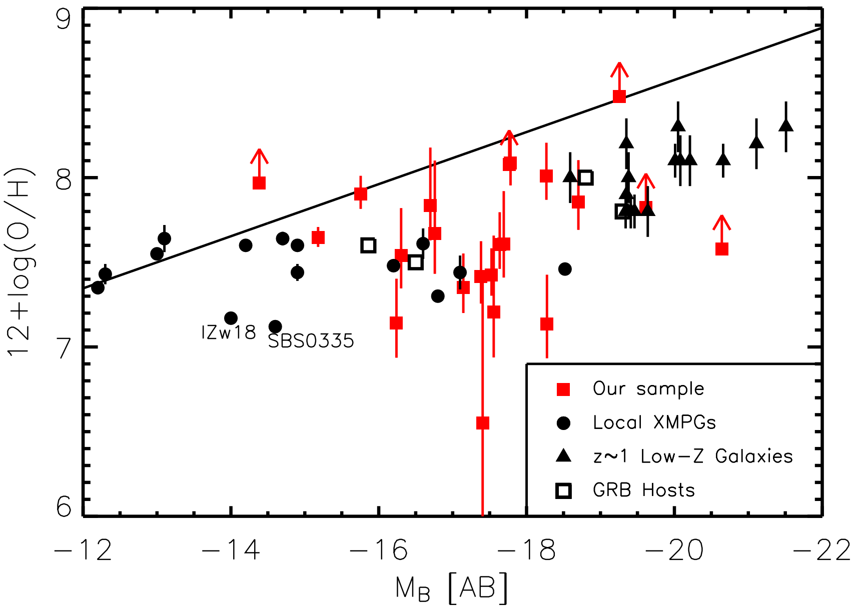

FIG. 19.— The oxygen abundance versus the absolute rest frame B magnitude for the [O III] selected samples (*red squares*). One sigma errors are shown for the oxygen abundances and one sigma lower limits are shown with upward pointing arrows. The solid line shows the (Skillman et al. 1989) relation for the nearby dwarf irregulars. As with the local XMPGs (*filled circles*, Kniazev et al. 2003; Kewley et al. 2007 and GRB hosts (open squares, Stanek et al. 2006; Kewley et al. 2007, the present galaxies are much more luminous at a given metallicity than the local irregulars. Metal-poor luminous galaxies (but not XMPGs) at $z \sim 1$ from Hoyos et al. 2005. are shown as triangles. A few of our emitters may have oxygen abundances comparable to the most metal-deficient galaxis, I Zw 18 (12 + log O/H = 7.17 ± 0.01, Thuan & Izotov 2005) and SBS 0335-052W (12 + log O/H = 7.12 ± 0.03, Izotov et al. 2005).

understand their frequency, that we are seeing objects undergoing continuous star formation rather than single starbursts. For the case of constant star formation with a standard Salpeter IMF a forming galaxy can have equivalent widths above 30Å for 10^9 yr (Leitherer et al. 1999) which would allows us to understand the observed number density of strong emitters relative to the total galaxy population.

In this type of model we would expect the metallicity to grow with time and that higher metallicity galaxies would have higher continuum magnitudes and lower equivalent widths in Hβ. We plot the absolute rest frame B magnitudes versus the Oxygen abundance in Figure 19. As with the case for the local XMPGs found in the SDSS (*filled circles*, Kniazev et al. 2003; Kewley et al. 2007) and the metal-poor galaxies ($7.8 < 12 + \log \mathrm{O/H} < 8.3$) at $z \sim 1$ (*triangles*, Hoyos et al. 2005), the present emitters (*red squares*) are much more luminous at a given metallicity than is found for the local dIrrs (*solid line*, Skillman et al. 1989). Furthermore there does indeed seem to be a trend to higher continuum luminosities at higher metallicity consistent with ongoing star formation raising the luminosity. Recently Kewley et al. (2007) reported the similarity between XMPGs and long duration GRB hosts ; they share similar SFRs, extinction levels, and both lie in a similar region of the luminosity-metallicity diagram. Our sample metal-deficient galaxies, which also lie in the region of GRB hosts, may be additional support of the connection between XMPGs and GRB hosts.

Of the six galaxies with continuum magnitudes brighter than -18 all but one have metallicities or lower limits which would place them near or above 12+log(O/H)=8 while the lower luminosity galaxies primarily have 12+log(O/H) in the range $7.1 - 7.8$. If we assumed that the metallicity were a simple linear function of the age then the more luminous galaxies would be several times older than the less luminous ones which is not quite enough to account for the luminosity increase (see e.g. Leitherer et al. 1999) suggesting that the enrichment process may be more complex. However, the accuracy of our current metallicity measurements may be inadequate for measuring the lowest metallicities in the sample and we could be underestimating the amount of metallicity evolution.

The relation between the metallicity and the Hβ equivalent width is shown in Figure 20. There clearly is a large scatter in metallicity at all equivalent widths suggesting that the star formation may be episodic with periods in which bursts of star formation enhances the Hβ equivalent widths in objects where previous star formation has raised the metallicity.

With better spectra and more accurate metal estimates we should be able to refine these tests and also determine whether the number density of objects versus metallicity is consistent with that expected in a simple growth model. Perhaps even more importantly as larger spectroscopic samples are obtained we should be able to determine if there is a floor on the metallicity corresponding to the enrichment in the intergalactic gas. Within the errors we have yet to find an object with lower metallicity than the lowest metallicity local galaxies but this could easily change as the observations are improved.

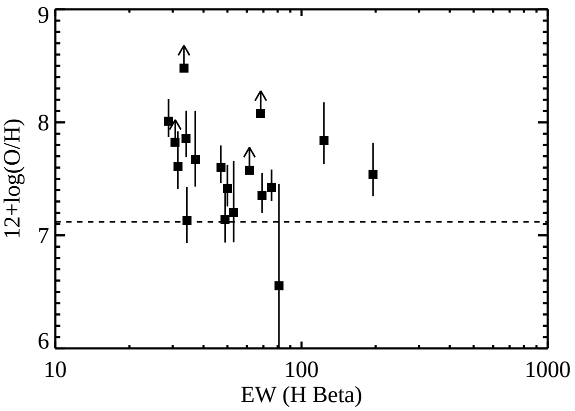

FIG. 20.— The oxygen abundance versus the rest frame Hβ equivalent width for the [O III] selected samples. One sigma errors are shown for the oxygen abundances and one sigma lower limits are shown with upward pointing arrows. The dotted line shows the metallicity of 1Zw-18.

9. SUMMARY

We have described the results of spectrscopic observations of a narrowband selected sample of extreme emission line objects. The results show that such objects are common in the $z = 0 - 1$ redshift interval and produce about 5-10% of the star formation seen in ultraviolet or emission line measurements at these redshifts. A very large fraction of the strong emitters are detected in the [O III]λ4363 line and oxygen abundances can be measured using the direct method. The abundance primarily lie in the 12+log(O/H) range of $7-8$ characteristic of XMPGs.

The results suggest that we are seeing early chemical enrichment of startup galaxies at these redshifts which are forming in relatively chemically regions. As we develop larger samples of these objects and improve the accuracy of their abundance estimates we should be able to test this model and to determine if there is a floor on the metallicity of the galaxies.

We are indebted to the staff of the Subaru and Keck observatories for their excellent assistance with the observations. We acknowledge Subaru/SuprimeCam support astronomer, Hisanori Furusawa, for his help over several years with the observations. Y. Kakazu acknowledges invaluable advice from Lisa J. Kewley and Roberto Terlevich on metallicity measurements. This work was supported in part by NSF grants AST04-07374 (LLC) and AST06-87850 (EMH), and Spitzer grant JPL 1289080 (EMH).

REFERENCES

Ajiki, M. et al. 2003. AJ, 126, 2091, astro-ph/0307325

Ajiki, M., et al. 2006, PASJ, 58, 113, astro-ph/0511471

Capak, P. et al. 2004, AJ, 127, 180, astro-ph/0312635

Corbin, M. R., Vacca, W. D., Cid Fernandes, R., Hibbard, J. E., Somerville, R. S., & Windhorst, R. A. 2006, ApJ, 651, 861, astro-ph/0607280

Cowie, L. L., Songaila, A., Hu, E. M., & Cohen, J. G. 1996, AJ, 112, 839, astro-ph/9606079

Faber, S. M. et al. 2003, Proc. SPIE, 4841, 1657

Garnett, D. R. 1992, AJ, 103, 1330

Giavalisco, M. et al. 2004, ApJ, 600, L93, astro-ph/0309105

Hoyos, C., Koo, D. C., Phillips, A. C., Willmer, C. N. A., & Guhathakurta, P. 2005, ApJ, 635, L21, astro-ph/0511066

Hu, E. M., Cowie, L. L., & McMahon, R. G. 1998, ApJ, 502, L99, astro-ph/9801003

Hu, E. M., Cowie, L. L., Capak, P., Hayashino, T., & Komiyama, Y. 2004, AJ, 127, 563, astro-ph/0311528

Hu, E. M., Cowie, L. L., Kakazu, Y., & Capak. P. 2007, in preparation

Izotov, Y. I., Thuan, T. X., & Guseva, N. G., 2005, ApJ, 415, 87, astro-ph/0506498

Izotov, Y. I., Papaderos, P., Guseva, N. G., Fricke, K. J., & Thuan, T. X. 2006a, A&A, 454, 137, astro-ph/0604234

Izotov, Y. I. 2006b, in ASP Conf. Ser. 353, Stellar Evolution at Low Metallicity: Mass Loss, Explosions, Cosmology, ed. H. J. G. L. M. Lamers, N. Langer, T. Nugis, & K. Annuk (San Francisco: ASP), 349

Izotov, Y. I., Stasińska, G., Meynet, G., Guseva, N. G., & Thuan, T. X. 2006c, A&A, 448, 955, astro-ph/0511644

Kennicutt, R. C., Jr. 1998, ARA&A, 36, 189, astro-ph/9807187

Kewley, L. J., & Dopita, M. A. 2002, ApJS, 142, 35, astro-ph/0206495

Kewley, L. J., Brown W. R., Geller, M. J., Kenyon, S. J., & Kurtz, M. J. 2007, ApJ, in press, astro-ph/0609246

Kniazev, A. Y., Grebel, E. K., Hao, L., Strauss, M. A., Brinkmann, J., & Fukugita, M. 2003, ApJ, 593, L73, astro-ph/0307401

Kobulnicky, H. A., & Kewley, L. J. 2004, ApJ, 617, 240, astro-ph/0408128

Kobulnicky, H. A., et al. 2003, ApJ, 599, 1006, astro-ph/0310346

Kunth, D., & Östlin, G. 2000, A&A Rev., 10, 1, astro-ph/9911094

Leitherer, C. et al. 1999, ApJS, 123, 3, astro-ph/9902334

Lilly, S. J., Carollo, C. M., & Stockton, A. N. 2003, ApJ, 597, 730, astro-ph/0307300

Ly, C. et al. 2007, ApJ, 657, 738, astro-ph/0610846

Maier, C., Lilly, S. J., Carollo, C. M., Meisenheimer, K., Hippelein, H., & Stockton, A. 2006, ApJ, 639, 858, astro-ph/0511255

Melbourne, J., & Salzer, J. J. 2002, AJ, 123, 2302, astro-ph/0202301

Miyazaki, S., et al. 2002, PASJ, 54, 833, astro-ph/0211006

Oey, M. S. 2006, in ASP Conf. Ser. 353, Stellar Evolution at Low Metallicity: Mass Loss, Explosions, Cosmology, ed. H. J. G. L. M. Lamers, N. Langer, T. Nugis, & K. Annuk (San Francisco: ASP), 253

Oke, J. B. 1990, AJ, 99, 1621

Osterbrock, D. E. 1989, Astrophysics of gaseous nebulae and active galactic nuclei (Mill Valley, CA: University Science Books)

Pagel, B.E.J., Simonson, E. A., Terlevich, R. J., & Edmunds, M. G. 1992, MNRAS, 255, 325

Papovich, C. et al. 2004, ApJ, 600, L111, astro-ph/0310888

Pilyugin, L. S. & Thuan, T. X. 2005, ApJ, 631, 231

Popescu, C. C., Hopp, U., Hagen, H. J., & Elsaesser, H. 1996, A&AS, 116, 43, astro-ph/9510127

Pustilnik, S. A., Engels, D., Kniazev, A. Y., Pramskij, A. G., Ugryumov, A. V., & Hagen, H.-J. 2006, Astronomy Letters, 32, 228, astro-ph/0508255

Salzer, J. J., et al. 2000, AJ, 120, 80, astro-ph/0004074

Sargent, W. L. W., & Searle, L. 1970, ApJ, 162, L155

Schiminovich, D., et al. 2005, ApJ, 619, L47, astro-ph/0411424

Schlegel, D. J., Finkbeiner, D. P., & Davis, M. 1998, ApJ, 500, 525, astro-ph/9710327, used to estimate dust extinctions from source location by the NASA/IPAC Infrared Science Archive Dust Reddening and Extinction Tool (`http://irsa.ipac.caltech.edu/applications/DUST/`)

Seaton M. J. 1975, MNRAS, 170, 475

Skillman, E. D., Kennicutt, R. C., & Hodge, P. W. 1989, ApJ, 347, 875

Stanek, K. Z. et al. 2006, Acta Astron., 56, 333, astro-ph/0604113

Stasińska, G., Schaerer, D., & Leitherer, C. 2002, Ap&SS, 281, 335

McMahon, R. G. 2003, MNRAS, 342, 439, astro-ph/0302212

Stern, D., Bunker, A., Spinrad, H., & Dey, A. 2000, ApJ, 537, 73, astro-ph/0002239

Stockton, A., & Ridgway, S. E. 1998, AJ, 115, 1340, astro-ph/9801056

Thuan, T. X., Izotov, Y. I. 2005, ApJS, 161, 240, astro-ph/0507209

Tran, K.-V. H., Lilly, S. J., Crampton, D., & Brodwin, M. 2004, ApJ, 612, L89, astro-ph/0407648

Turnshek, D. A., Bohlin, R. C., Williamson II, R. L., Lupie, O. L., Koornneef, J., & Morgan, D.H. 1990, AJ, 99, 1243

Ugryumov, A. V., et al. 1999, A&AS, 135, 511

Wilson, G., Cowie, L. L., Barger, A. J., & Burke, D. J. 2002, AJ, 124, 1258, astro-ph/0203168

Wyder, T. K., et al. 2005, ApJ, 619, L15, astro-ph/0411364

TABLE 2
NB816 Emission-Line Sample

No.	RA(2000)	Dec(2000)	$N(AB)$	$Z(AB)$	I	R	V	B	z
1	40.115555	−1.694722	23.92	25.28	24.84	25.44	−99.00	−99.00	−1.0000
2	40.116665	−1.617361	24.26	25.88	25.52	25.74	−99.00	−99.00	−1.0000
3	40.138332	−1.405639	23.49	24.94	24.70	25.22	−99.00	−99.00	0.6343
4	40.174721	−1.704750	24.27	25.46	25.35	25.82	−99.00	−99.00	0.6355
5	40.183056	−1.495417	24.58	25.28	25.85	26.86	−99.00	−99.00	5.6886
6	40.216946	−1.494805	24.80	26.08	26.31	26.14	−99.00	−99.00	0.2416
7	40.250832	−1.744639	23.51	24.35	24.33	24.54	−99.00	−99.00	−1.0000
8	40.276112	−1.518139	24.72	24.78	25.53	25.75	−99.00	−99.00	−1.0000
9	40.276390	−1.623250	24.55	25.36	25.36	25.76	−99.00	−99.00	−1.0000
10	40.284168	−1.453583	21.82	23.20	23.02	22.56	−99.00	−99.00	0.2480
11	40.298889	−1.447389	24.32	25.95	25.42	25.71	−99.00	−99.00	−1.0000
12	40.304165	−1.391694	20.88	22.35	22.06	22.32	−99.00	−99.00	−1.0000
13	40.306946	−1.638500	24.91	25.67	25.72	26.02	−99.00	−99.00	−1.0000
14	40.311111	−1.535111	24.08	25.93	25.49	25.71	−99.00	−99.00	0.6240
15	40.318333	−1.548222	24.60	25.03	25.50	25.96	−99.00	−99.00	−1.0000
16	40.318890	−1.430889	23.37	23.77	24.32	24.42	−99.00	−99.00	1.1804
17	40.319168	−1.446333	23.60	23.85	24.43	24.56	−99.00	−99.00	1.1873
18	40.320835	−1.778028	20.70	21.57	21.60	21.86	−99.00	−99.00	−1.0000
19	40.324165	−1.409972	24.29	24.38	25.18	25.45	−99.00	−99.00	−1.0000
20	40.326111	−1.709805	23.24	24.75	24.62	24.96	−99.00	−99.00	−1.0000
21	40.336388	−1.570194	24.26	24.73	25.06	25.33	−99.00	−99.00	−1.0000
22	40.337223	−1.388194	24.81	27.37	26.71	26.77	−99.00	−99.00	−1.0000
23	40.337502	−1.658306	24.89	25.20	25.76	26.05	−99.00	−99.00	−1.0000
24	40.340279	−1.689472	24.55	26.37	26.07	26.51	−99.00	−99.00	−1.0000
25	40.340557	−1.551889	24.99	25.70	25.93	26.35	−99.00	−99.00	−1.0000
26	40.340832	−1.371222	22.42	23.43	23.29	23.16	−99.00	−99.00	−1.0000
27	40.340832	−1.516250	24.89	25.06	25.69	25.78	−99.00	−99.00	−1.0000
28	40.341110	−1.493500	23.37	24.62	24.55	24.23	−99.00	−99.00	−1.0000
29	40.341389	−1.484139	24.48	25.46	25.49	25.73	−99.00	−99.00	−1.0000
30	40.342777	−1.599528	24.65	25.31	25.50	25.85	−99.00	−99.00	−1.0000
31	40.343056	−1.438833	23.17	24.60	24.54	24.54	−99.00	−99.00	0.6226
32	40.347500	−1.403833	24.86	27.45	26.16	26.35	−99.00	−99.00	0.6324
33	40.349724	−1.598472	23.11	23.87	24.11	24.46	−99.00	−99.00	1.1956
34	40.356388	−1.515722	24.94	26.19	26.18	26.42	−99.00	−99.00	−5.0000
35	40.372223	−1.390361	23.85	24.68	24.72	24.62	−99.00	−99.00	−1.0000
36	40.373611	−1.722528	24.93	25.85	25.74	25.88	−99.00	−99.00	−1.0000
37	40.377777	−1.701889	23.45	23.82	24.26	24.70	−99.00	−99.00	−1.0000
38	40.388054	−1.697361	23.96	24.32	24.79	24.90	−99.00	−99.00	−1.0000
39	40.388889	−1.573361	24.79	25.13	25.65	26.07	−99.00	−99.00	−1.0000
40	40.394444	−1.521389	22.73	23.69	23.84	24.06	−99.00	−99.00	0.6292

Note. — Magnitudes are measured in $3''$ diameter apertures. An entry of '−99' indicates that no excess flux was measured. −1.0000 in the redshift column means no spectroscopic data were obtained for the object. This is a sample table showing the first entries of the electronic version of the table that will accompany the published paper.

TABLE 3
NB912 Emission-Line Sample

No. (1)	R.A. (J2000.0) (2)	Decl. (J2000.0) (3)	$N(AB)$ (4)	$z'(AB)$ (5)	I (6)	R (7)	V (8)	B (9)	z_{spec} (10)
1	40.131668	−1.408361	23.86	25.08	25.89	25.97	−99.00	−99.00	0.8371
2	40.133888	−1.575222	24.76	25.92	26.13	25.84	−99.00	−99.00	1.4498
3	40.148056	−1.593555	23.21	24.62	25.53	26.11	−99.00	−99.00	0.8207
4	40.148335	−1.725417	24.76	25.97	26.98	26.39	−99.00	−99.00	0.8111
5	40.150833	−1.737556	23.31	24.35	24.88	25.32	−99.00	−99.00	0.8269
6	40.153332	−1.536833	23.64	25.00	26.18	26.87	−99.00	−99.00	0.8301
7	40.156387	−1.765833	21.93	23.05	23.51	23.74	−99.00	−99.00	−1.0000
8	40.165833	−1.580056	24.94	26.20	25.92	25.84	−99.00	−99.00	1.4482
9	40.183334	−1.389583	21.77	22.79	23.33	23.52	−99.00	−99.00	0.8325
10	40.184444	−1.596444	23.09	24.50	25.30	25.55	−99.00	−99.00	0.8293
11	40.193611	−1.690083	24.32	25.40	25.83	25.69	−99.00	−99.00	0.8266
12	40.194168	−1.373722	23.93	24.93	25.21	25.35	−99.00	−99.00	−1.0000
13	40.194721	−1.373917	24.87	25.90	26.30	26.47	−99.00	−99.00	−1.0000
14	40.196667	−1.378333	24.07	25.42	26.05	26.18	−99.00	−99.00	−1.0000
15	40.202221	−1.584472	24.22	25.30	25.81	26.19	−99.00	−99.00	0.8289
16	40.203335	−1.471861	24.77	26.20	25.78	25.54	−99.00	−99.00	0.3965
17	40.214722	−1.519917	23.14	24.40	25.38	25.94	−99.00	−99.00	0.8288
18	40.220276	−1.753778	24.34	25.41	26.40	26.29	−99.00	−99.00	−1.0000
19	40.220833	−1.388556	23.24	24.36	25.13	24.99	−99.00	−99.00	−1.0000
20	40.226944	−1.542111	23.02	24.47	25.77	25.48	−99.00	−99.00	0.8208
21	40.229168	−1.720889	24.99	27.85	27.11	···	−99.00	−99.00	6.4800
22	40.229443	−1.376472	23.75	24.98	25.72	24.66	−99.00	−99.00	−1.0000
23	40.245834	−1.578972	24.61	25.82	27.22	26.91	−99.00	−99.00	0.8285
24	40.280556	−1.421056	24.82	25.86	26.13	25.91	−99.00	−99.00	−1.0000
25	40.290833	−1.746361	23.89	25.16	25.81	25.03	−99.00	−99.00	0.0000
26	40.323891	−1.697667	24.73	25.80	26.47	25.71	−99.00	−99.00	−1.0000
27	40.330833	−1.612389	23.03	24.68	26.06	25.47	−99.00	−99.00	0.0000
28	40.339722	−1.395361	23.87	25.54	26.98	25.45	−99.00	−99.00	0.3889
29	40.346668	−1.448305	23.93	24.98	25.37	25.48	−99.00	−99.00	0.8274
30	40.382500	−1.554056	23.52	24.87	25.60	25.08	−99.00	−99.00	0.3930
31	40.393055	−1.713694	24.94	26.83	26.70	26.50	−99.00	−99.00	−1.0000
32	40.398888	−1.466417	23.87	24.91	24.83	24.64	−99.00	−99.00	1.4590
33	40.403889	−1.530167	24.88	26.08	27.44	27.30	−99.00	−99.00	0.8223
34	40.409443	−1.369222	21.52	23.44	24.47	24.04	−99.00	−99.00	−1.0000
35	40.411667	−1.691417	24.41	25.50	25.68	25.55	−99.00	−99.00	−1.0000
36	40.424999	−1.454028	21.91	22.93	23.42	23.41	−99.00	−99.00	−1.0000
37	40.430000	−1.501111	23.13	24.21	24.76	24.92	−99.00	−99.00	0.8267
38	40.446110	−1.676139	24.91	26.09	26.37	26.04	−99.00	−99.00	−1.0000
39	40.478889	−1.534278	24.87	26.06	25.79	25.56	−99.00	−99.00	0.3861
40	40.506111	−1.755111	22.73	24.27	25.24	25.19	−99.00	−99.00	−1.0000
41	40.511665	−1.596944	24.73	25.96	25.55	25.67	−99.00	−99.00	−1.0000
42	40.518055	−1.666139	22.47	23.73	24.37	24.45	−99.00	−99.00	−1.0000

Note. — Magnitudes are measured in $3''$ diameter apertures. An entry of '-99' indicates that no excess flux was measured. -1.0000 in the redshift column means no spectroscopic data were obtained for the object. This is a sample table showing the first entries of the electronic version of the table that will accompany the published paper.

TABLE 4
Line fluxes and Oxygen Abundance for L816 selected emitters

Object	f([OIII]5007)	f([OIII]4959)	f([OIII]4363)	f([OII]3727)	T_e[OIII]	12+log(O/H)
[OIII] emitters						
31	513.6 ± 24.0	222.3 ± 11.4	< 6.60	54.4 ± 4.62	< 1.19	> 8.09
40	577.9 ± 21.6	191.3 ± 8.05	9.40 ± 3.40	140.9 ± 6.22	$1.14 < 1.34 < 1.53$	$7.86 < 8.03 < 8.25$
51	401.5 ± 12.6	146.9 ± 5.52	9.40 ± 4.50	< 2.39	$1.19 < 1.55 < 1.90$	$7.51 < 7.62 < 7.94$
76	464.4 ± 10.5	191.3 ± 4.86	< 2.90	344.5 ± 8.07	< 0.95	> 8.55
118	492.6 ± 29.7	193.9 ± 12.9	34.4 ± 12.8	11.3 ± 2.61	$2.16 < 3.08 < 4.32$	$6.93 < 7.16 < 7.44$
195	335.0 ± 21.4	129.5 ± 10.2	24.0 ± 10.9	97.1 ± 9.71	$2.02 < 3.17 < 4.86$	$6.78 < 7.06 < 7.44$
206	597.1 ± 19.5	204.1 ± 7.41	21.6 ± 9.20	< 1.72	$1.48 < 1.97 < 2.48$	$7.42 < 7.55 < 7.84$
208	658.0 ± 30.9	249.8 ± 12.3	15.6 ± 8.00	< 22.1	$1.16 < 1.56 < 1.93$	$7.67 < 7.85 < 8.22$
223	242.9 ± 15.3	83.3 ± 7.53	23.7 ± 18.9	< 10.1	$1.45 < 4.64 < 19.62$	$6.14 < 6.61 < 7.53$
252	466.8 ± 9.32	157.9 ± 3.57	9.20 ± 4.00	139.0 ± 3.71	$1.16 < 1.45 < 1.72$	$7.68 < 7.87 < 8.14$

Note. — Only emitters with $> 15\sigma$ Hβ fluxes are listed. All fluxes are normalized by their f(Hβ) and multiplied by 100. 1σ upper limits are listed for [OII]3727 flux below 3σ and [OIII]4363 below 1σ. The units of T_e[OIII] are 10^{-4} [K].

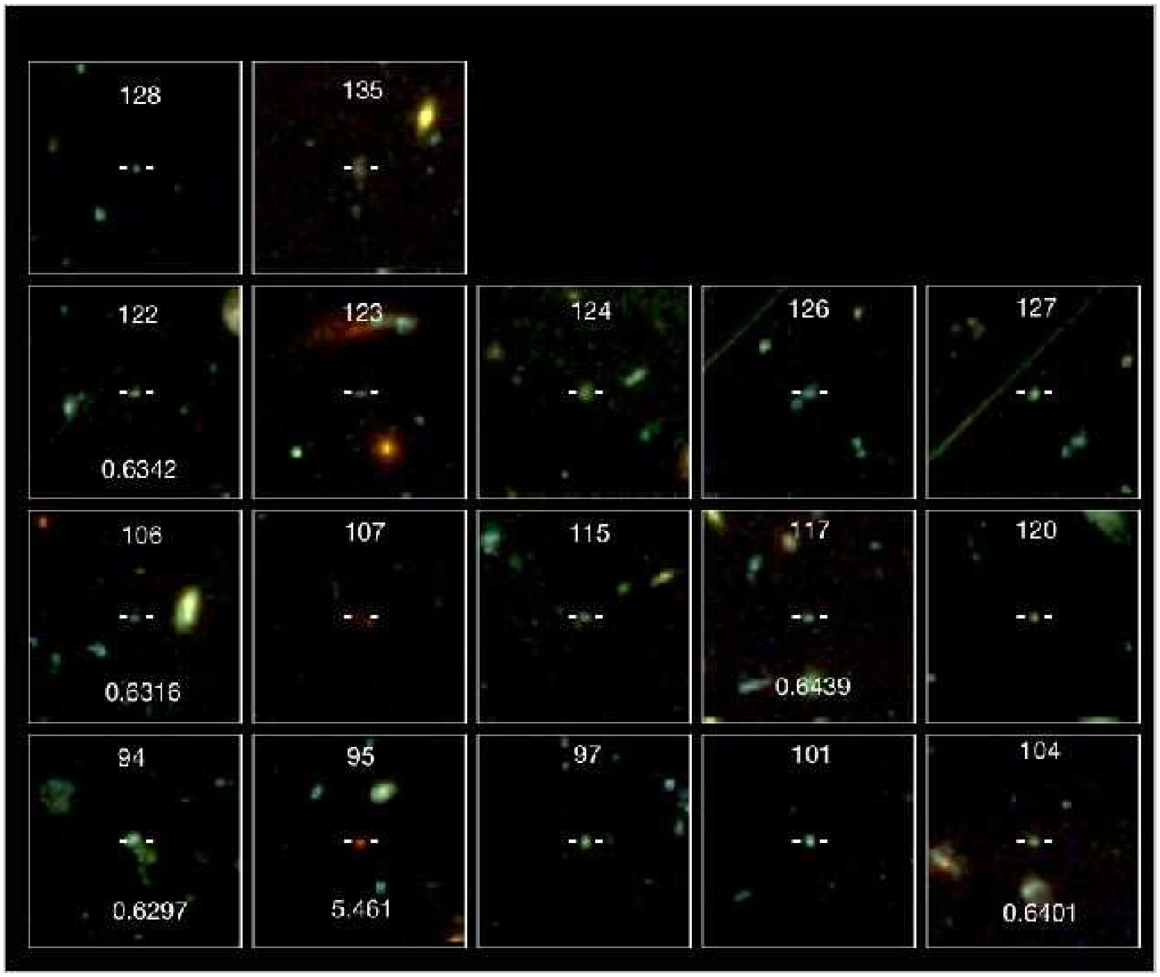

FIG. 17.— HST/ACS (B, V, z') composite images of NB816 emitters in the GOODS-N field with overlaid object IDs from Table 2 and redshifts, where known. Fields are 12.″5 on a side.

TABLE 5

LINE FLUXES AND OXYGEN ABUNDANCES FOR L912 SELECTED EMITTERS

Object	f([OIII]5007)	f([OIII]4959)	f([OIII]4363)	f([OII]3727)	T_e[OIII]	12+log(O/H)
[OIII] emitters						
3	550.9 ± 12.9	187.9 ± 4.91	23.9 ± 7.90	8.6 ± 2.5	$1.74 < 2.20 < 2.71$	$7.26 < 7.43 < 7.65$
6	588.1 ± 35.1	216.0 ± 14.2	18.4 ± 11.0	52.0 ± 8.6	$1.20 < 1.79 < 2.39$	$7.40 < 7.68 < 8.14$
9	442.3 ± 15.3	154.7 ± 6.42	< 12.3	157.2 ± 6.88	< 1.70	> 7.70
10	490.0 ± 11.9	178.7 ± 5.14	13.7 ± 4.40	< 2.95	$1.42 < 1.69 < 1.97$	$7.55 < 7.61 < 7.82$
17	342.5 ± 20.0	129.7 ± 9.29	15.9 ± 9.40	< 7.72	$1.41 < 2.26 < 3.28$	$7.03 < 7.22 < 7.70$
20	418.7 ± 17.4	135.1 ± 6.96	16.8 ± 5.50	24.5 ± 2.45	$1.69 < 2.11 < 2.57$	$7.18 < 7.36 < 7.58$
239	202.4 ± 10.2	75.6 ± 6.40	< 8.20	190.6 ± 10.2	< 2.08	> 7.34
270	351.7 ± 15.1	149.7 ± 7.73	12.4 ± 3.40	30.7 ± 2.72	$1.59 < 1.87 < 2.16$	$7.28 < 7.43 < 7.61$
Hα emitters						
52	589.1 ± 10.0	179.2 ± 3.42	18.3 ± 1.59	< 1.56	$1.75 < 1.83 < 1.92$	$7.62 < 7.67 < 7.72$
60	619.1 ± 33.5	206.7 ± 12.5	10.7 ± 7.77	48.4 ± 8.7	$0.90 < 1.37 < 1.77$	$7.67 < 7.96 < 8.57$
266	682.8 ± 10.3	217.7 ± 3.57	14.7 ± 2.42	...	$1.40 < 1.52 < 1.63$	< 8.3

NOTE. — Same as Table 4 but for NB912 emitters. The [OII]λ3727 of ID266 is beyond the DEIMOS wavelength coverage and thus was not being measured.

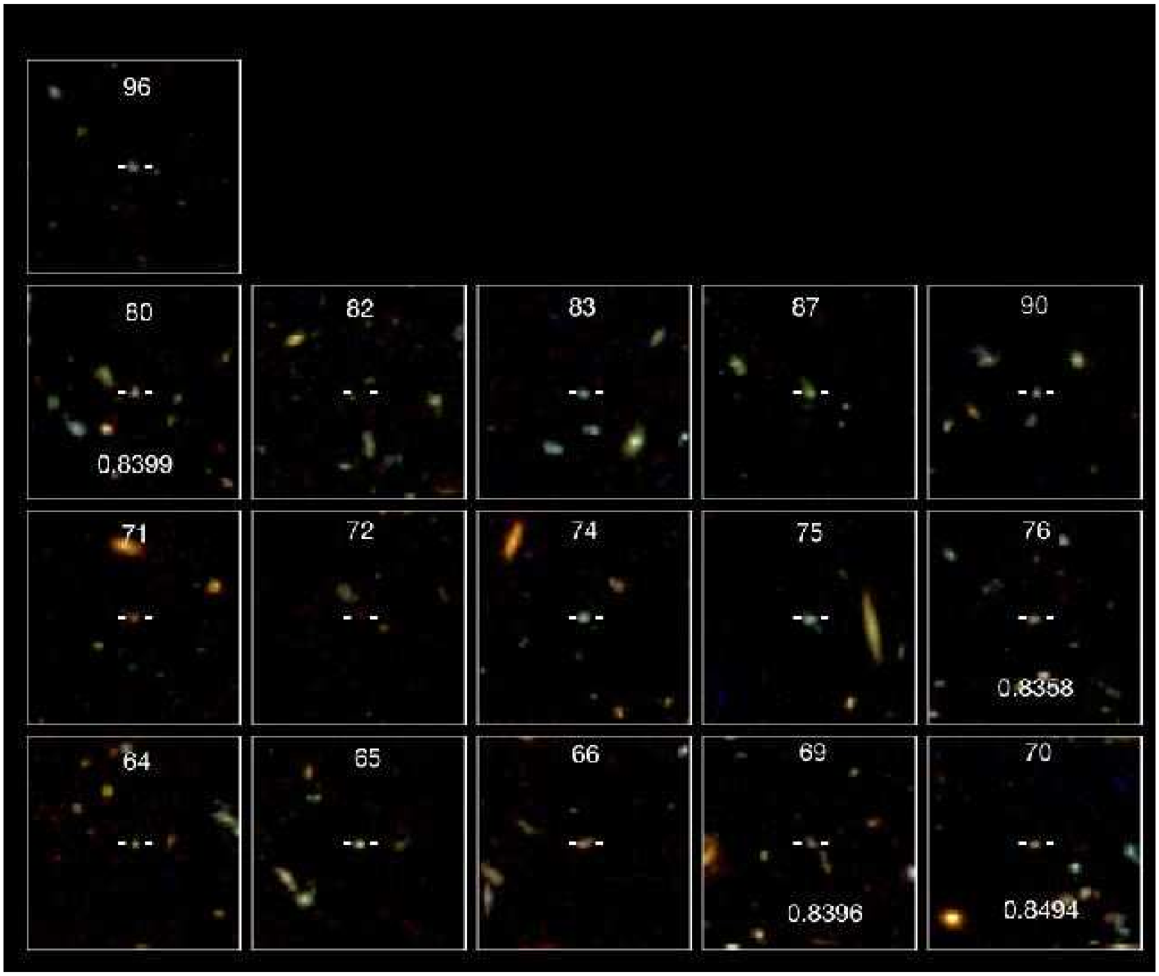

FIG. 18.— HST/ACS (B, V, I) composite images of NB912 emitters in the GOODS-N field with overlaid object IDs from Table 3 and redshifts, where known. Fields are 12.″5 on a side.